Thermoelectric properties of Sb-doped tin oxide by a one-step solid-state reaction

Leilane R. Macario [a,b,*], Andrew Golabek [b], Holger Kleinke [b], Edson R. Leite [a,c]

[a] Brazilian Nanotechnology National Laboratory (LNNano), CNPEM, Campinas, SP, 13083-970, Brazil
[b] Department of Chemistry and Waterloo Institute for Nanotechnology, University of Waterloo, Waterloo, ON N2L 3G1, Canada
[c] Chemistry Department, CDMF, LIEC, Federal University of São Carlos, São Carlos, SP, 13565-905, Brazil

ABSTRACT

Recently, oxide-based materials have proven to be potential thermoelectric materials at high temperatures. In this work, the thermoelectric properties of one-step solid-state sintered Sn$_{1-x}$Sb$_x$O$_2$ (x = 0, 0.005, 0.01, 0.02, 0.03, 0.04) ceramic pellets were investigated in detail. It was confirmed that the addition of Sb significantly alters the thermoelectric properties of SnO$_2$ due to the increase in the carrier concentration, which increases the electrical conductivity. The Seebeck coefficient values of all the solid solutions were negative, which indicates that these samples have n-type conduction. The thermoelectric performance of the material was evaluated by determining the zT value and the best composition was Sn$_{0.98}$Sb$_{0.02}$O$_2$ with zT ~0.06 at 1073 K.

1. Introduction

Nowadays, the search for a thermoelectric efficient system comprised of low-cost materials, with considerable compatibility with current technology, is of great importance. Approximately 60% of energy resources are discharged as waste heat into the environment [1]. Therefore, novel thermoelectric materials that convert waste heat from a temperature gradient into electrical energy have received much attention [2,3]. The performance of thermoelectric materials is determined by the dimensionless figure of merit zT [4], where T is the absolute temperature and $z = S^2 \sigma \kappa^{-1}$ (where S is the Seebeck coefficient, σ the electrical conductivity, and κ the total thermal conductivity).

The traditional thermoelectric materials [5] [–] [9] are unstable at higher temperatures or are vulnerable to sublimation or oxidation. Furthermore, these thermoelectric materials are made from elements that are either scarce in the earth's crust or toxic (e.g. Pb, Sb, Bi and Te). Thermoelectric materials based on oxides containing earth-abundant and non-toxic elements are a potential solution to the stability and toxicity concerns, as oxides are normally stable at high temperatures and in oxidizing atmospheres. However, oxide-based thermoelectrics tend to have relatively low zT values mainly due to their larger lattice thermal conductivities and lower mobilities compared to traditional thermoelectric materials like chalcogenides and pnictides [10,11]. Several new strategies have been applied to oxides in order to increase the figure of

merit, including dimensionality reduction, with which low total thermal conductivity values between ~1 and ~1.5 W m^{-1}K^{-1} were achieved for indium tin oxide nanowires [12], complex composites, e.g. Na$_x$CoO$_2$/Co$_3$O$_4$ layered nano-composite showed a significant increase in electrical conductivity above 750 K, and it reached 1.2×10^2 Ω^{-1}cm^{-1} at 1200 K [13], introductions of impurity states in the bulk phase, e.g. dopants at the Sr-site in strontium titanate were used to improve its thermoelectric performance resulting in Sr$_{0.87}$Dy$_{0.07}$Nd$_{0.06}$TiO$_3$ with a zT of 0.19 at 673 K [14], and multiple doping in the tin oxide matrix resulted in a maximum power factor of 4.8×10^{-4} W m^{-1}K^{-2} at 1060 K for Sn$_{0.97}$Sb$_{0.01}$Zn$_{0.01}$Bi$_{0.01}$O$_2$ and 1.2×10^{-4} W m^{-1}K^{-2} at 1073 K for Sn$_{0.9}$Sb$_{0.05}$Zn$_{0.05}$O$_2$ [15,16].

Tin dioxide SnO$_2$ crystallizes in the rutile structure with the space group $P4_2/mnm$, with room temperature lattice parameters of $a = b = 4.737$ Å and $c = 3.186$ Å, and exhibits a bandgap of $E_g = 3.57$ eV [17]. SnO$_2$ materials have been widely applied in various fields such as optoelectronic devices [18,19], solar cells [20] and gas sensors [17,21], due to their excellent chemical and thermal stabilities and superior optical and electrical properties. In the past few years, various reports on the synthesis of SnO$_2$ have been presented, including sol-gel synthesis [22], laser decomposition reactions [23], and hydrothermal methods [24]. All of these methods are suitable for synthesis, although with limitations, i.e. the need for a complex apparatus, difficult techniques and process controls as well as high cost. In this work, we report a simple

---

* Corresponding author. Brazilian Nanotechnology National Laboratory (LNNano), CNPEM, Campinas, SP, 13083, Brazil.
  E-mail address: leilane.macario@lnnano.cnpem.br (L.R. Macario).

one-step solid-state reaction route to prepare SnO_2, which is carried out in air, in a dispensing solvent and is also attractive because of its low cost. The reports related to the thermoelectric properties of this material are scarce. Some doping and alloying approaches have been performed from the discovery of this thermoelectric oxide, leading to the exploration of new compositions, such as $Sn_{0.99}Sb_{0.01}O_2$ [25] or $Sn_{0.97}Sb_{0.01}Zn_{0.01}M_{0.01}O_2$ [16]. However, these studies either do not report the zT values and/or the materials are not obtained by the conventional solid-state method, using equipment that makes the experimental procedure more costly. Thus, this work includes extensive knowledge of thermoelectric properties of $Sn_{1-x}Sb_xO_2$ (x = 0, 0.005, 0.01, 0.02, 0.03, 0.04). Undoped SnO_2 has low electrical conductivity and carrier concentration. Therefore, we investigated doping with antimony oxide to improve the electrical properties [15,16,26–28]. Consequently, different approaches can be performed from the results observed in this study to improve thermoelectric properties of Sb-doped SnO_2 materials, using a relatively simple and economical method.

The purpose of this work is to optimize the temperature dependence of the thermoelectric properties of Sb-doped SnO_2 obtained by a one-step solid-state reaction over an ample temperature range and evaluate the potential for an application in a thermoelectric power generator.

2. Experimental details

The one-step solid-state synthesis was conducted to obtain single-phase antimony-doped tin oxide pellets. $Sn_{1-x}Sb_xO_2$ (x = 0, 0.005, 0.01, 0.03, 0.04) ceramics were prepared from the fine powders of SnO_2 (99%, Merck) and Sb_2O_3 (99%, Aldrich). Stoichiometrically weighed powders were mixed in a planetary ball mill for 20 min and pressed into pellets of a diameter of 12.7 mm at a pressure of 60 MPa at room temperature. The pellets were heated at 1573 K for 24 h in air in a tube furnace.

3. Characterizations

The crystal structure of these materials was determined on a D8 Advance ECO Bruker powder X-ray diffractometer. Rietveld refinements were performed using the program GSAS EXPGUI [29,30]. A Lorentzian anisotropic size broadening (spherical harmonics) model was applied to calculate the accurate sizes of the crystallites considering the anisotropy in the particles.

The pellets were used to determine the thermal diffusivity, measured between 373 and 1073 K under an argon atmosphere using a TA Instruments DLF 1200 thermal properties analyzer. The thermal conductivities were derived from the thermal diffusivity a, the heat capacity C_p as calculated via the Dulong−Petit approximation, and the experimental density ρ of the sintered pellets as determined via the Archimedes method, via $\kappa = a\, C_p\, \rho$.

Afterwards, the pellets were cut into a square shape with the dimensions of 9×9 mm^2 and Hall measurements were conducted using a Hall Effect measurement system (Nanomagnetics Instruments, model ezHEMS) at room temperature.

Then, the pellets were cut into rectangular bars with the dimensions of $9 \times 2 \times 2$ mm^3, which were used to determine the electrical conductivities and the Seebeck coefficients using an ULVAC-RIKO ZEM-3 apparatus, measuring from 373 to 1073 K under a helium atmosphere. The figure of merit was calculated from the values obtained by the above measurements. The experimental errors were estimated to be ±5% for σ, ±5% for S, ±5% for κ, and thus ±10% for the figure of merit, zT.

4. Results and discussions

The X-ray diffraction pattern of the pristine and Sb-doped samples, $Sn_{1-x}Sb_xO_2$ (x = 0, 0.005, 0.01, 0.02, 0.03, 0.04), prepared via solid-state reaction were assigned to the tetragonal cassiterite phase of SnO_2
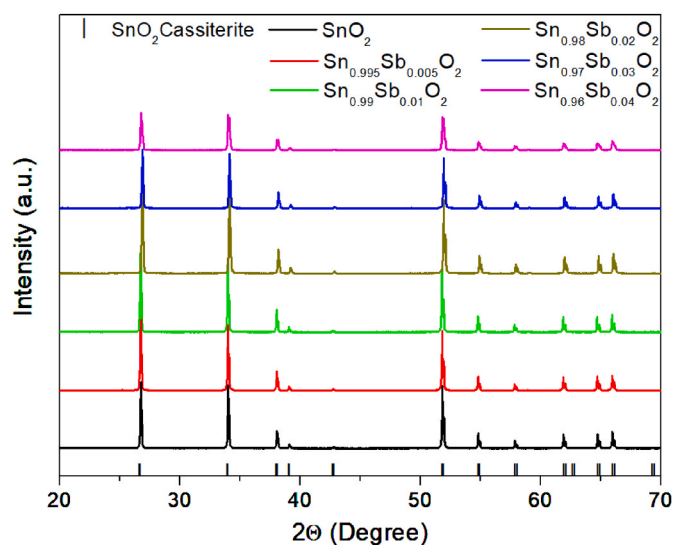

Fig. 1. X-ray diffraction patterns of $Sn_{1-x}Sb_xO_2$ (x = 0, 0.005, 0.01, 0.02, 0.03, 0.04) solid solutions.

Table 1
Rietveld refinement values of lattice parameters and crystallite sizes.

Nominal composition of Sb	Average crystallite size (nm)	Lattice Parameter $a = b$ (Å)	Lattice Parameter c (Å)	Cell Volume V (Å^3)
0	34	4.74957(4)	3.19471(3)	72.068(1)
0.5	29	4.74958(4)	3.19500(3)	72.074(2)
1	24	4.74964(4)	3.19505(3)	72.078(2)
2	20	4.74974(3)	3.19521(2)	72.084(1)
3	19	4.75048(2)	3.19622(3)	72.129(2)
4	19	4.75037(5)	3.19615(6)	72.124(2)

(PDF#41–1445), confirming the formation of phase-pure SnO_2 with Sb being incorporated into the crystal structure (Fig. 1). Rietveld refinements were used to obtain the lattice parameters and sizes of the crystallites as shown in Table 1.

A small increase in the lattice parameters a and c while the c/a ratio remained constant was observed with increasing Sb content (see Table 1). This enhancement in lattice parameters resulted in an increase in the volume of the unit cell with increasing Sb concentration [31–33].

A Lorentzian anisotropic size broadening with the spherical harmonics model was used to calculate the dimensions of the crystallites. It is evident that as the antimony oxide content increases, the crystallite dimensions slightly decrease from about 34 nm (pristine) to 19 nm (4% mol Sb; x = 0.04). This reduction in crystallite size might be due to the solute drag effect [34] that reduces the mobility of SnO_2 grain boundaries due to the increasing amount of Sb^{3+} segregation on the surfaces of ceramic grains. Another possible explanation is that the distortion in the crystalline lattice is caused by the presence of Sb atoms in interstitial positions, which makes the diffusion processes more difficult [26,31, 32]. The presence of Sb seems to change the particle size and morphology by increasing the formation of aggregates, showing that chemical composition affects the morphology of the SnO_2 phase (Fig. 2). The Sb-free SnO_2 consists of highly agglomerated particles with diameters of approximately 600 nm, while $Sn_{0.98}Sb_{0.02}O_2$ consists of highly agglomerated particles with diameters of approximately 460 nm and less agglomerated particles with facets with diameters of approximately 1350 nm.

Fig. 3(a) illustrates the variation in the mobility and carrier concentration of the $Sn_{1-x}Sb_xO_2$ (x = 0, 0.005, 0.01, 0.02, 0.03, 0.04) solid solutions as a function of the Sb content. A conceivable increase in the carrier concentration with increasing Sb content can be noticed, with the
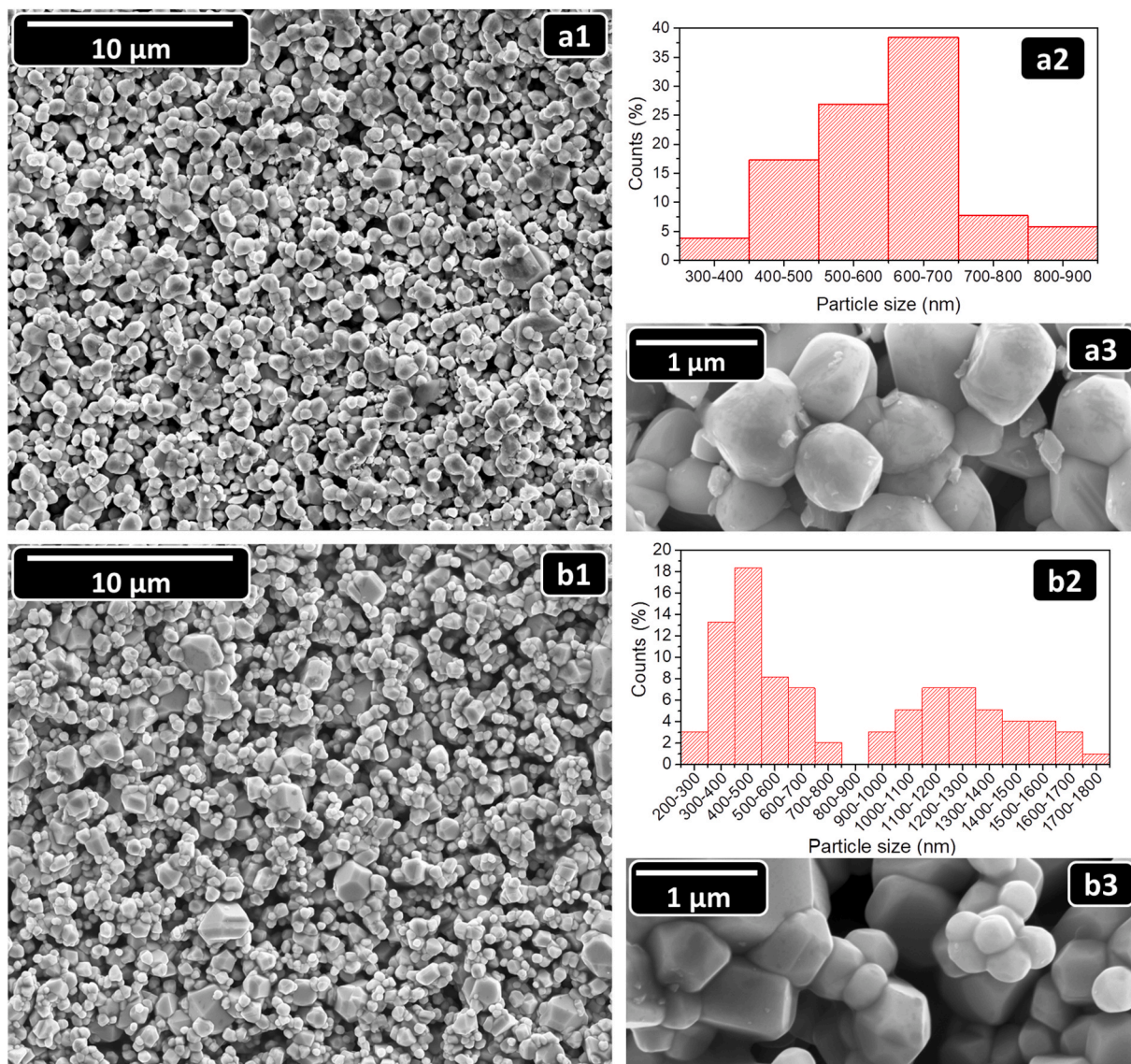
Fig. 2. SEM pictures of (a1, a3) SnO$_2$ and (b1, b3) Sn$_{0.98}$Sb$_{0.02}$O$_2$ pellet surfaces, and histograms of average particle sizes of (a2) SnO$_2$ and (b2) Sn$_{0.98}$Sb$_{0.02}$O$_2$.
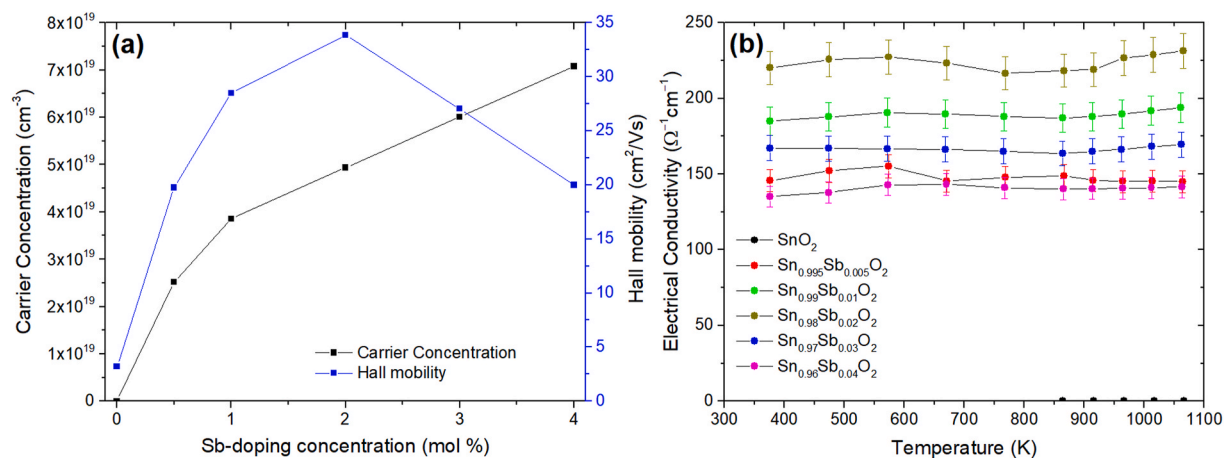

Fig. 3. (a) Hall measurement results (mobility and carrier concentration) and (b) temperature dependence of the electrical conductivity of Sn$_{1-x}$Sb$_x$O$_2$ (x = 0, 0.005, 0.01, 0.02, 0.03, 0.04).
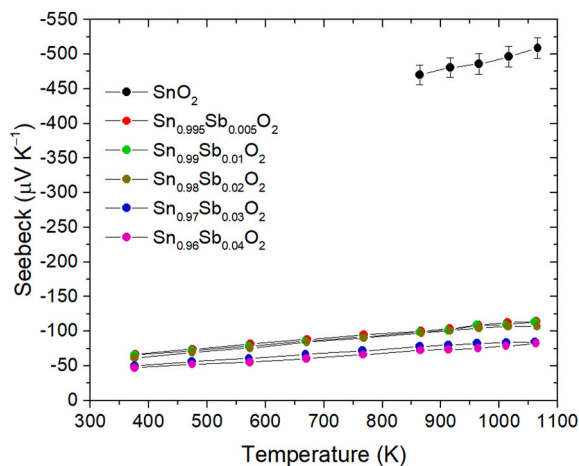
Fig. 4. Temperature dependence of the Seebeck coefficient of $Sn_{1-x}Sb_xO_2$ (x = 0, 0.005, 0.01, 0.02, 0.03, 0.04).

maximum being 7.1×10^{19} cm^{-3} at x = 0.04. Sb^{5+} ions act as the electron donor being added to SnO_2, increasing the carrier concentration. Specifically, 0.01 Sb^{5+} per formula unit would hypothetically add 3.3×10^{19} electrons per cm^3. Such a concentration was actually achieved with x = 0.01, but adding more Sb resulted in smaller increases of the carrier concentration. The different carrier concentrations may be a consequence of the Sb mixed valence and segregation as explained below.

The carrier mobility initially increased with Sb doping, reaching its maximum of 33.4 cm^{2}V^{-1}s^{-1} at x = 0.02, beyond which it gradually decreased. During the initial addition of Sb into the SnO_2 matrix, Sb^{5+} ions are incorporated at Sn^{4+} sites acting as donors, creating excess electrons. The decreasing charge mobility with upper doping concentrations (x > 0.02) is mainly attributed to increased extra ionized impurity scattering. In addition, the reduced crystallite size with increasing x, and thus increased amount of grain boundary regions, forms a potential barrier, impeding the migration of carriers between crystallites. This is in agreement with the X-ray diffraction results, showing that the crystallite size decreases and subsequently the grain boundary regions are enhanced with the increase in antimony concentration; therefore, the ability of grain boundary scattering is increasing in addition to the extra ionized impurity scattering.

The variation in the carrier mobility manifests itself in a variation in the electrical conductivity of the $Sn_{1-x}Sb_xO_2$ samples. The electrical conductivity increased from x = 0 to x = 0.02, reaching a maximum of

231 Ω^{-1}cm^{-1} at 1073 K, to then decrease with increasing x because of the decreasing mobility, as presented in Fig. 3(b). Fan et al. [35] observed similar behavior in Sb-doped SnO_2 ceramics. The electrical conductivity increased from x = 2 to x = 8, reaching a maximum of ~20 Ω^{-1}cm^{-1} at room temperature, then decreases with x = 10 as mobility decreases. The electrical conductivity values found here are competitive, for example in comparison to post-annealing Zn_2AlO_4 (44 Ω^{-1}cm^{-1} at room temperature), Zn_2SnO_4 (55 Ω^{-1}cm^{-1} at room temperature) [36], $In_{1.9}Mo_{0.1}O_3$ (~12 Ω^{-1}cm^{-1} at 1073 K) [37], and $CaMnO_3$ (~17.5 Ω^{-1}cm^{-1} at 873 K) [38].

After doping with Sb, the temperature dependence of the electrical conductivity varied from semiconductor-like transport behavior to semi-metal-like behavior, with almost no temperature dependence. Several authors described similar variations in electrical conductivity with enhancing Sb content in the SnO_2 matrix, principally attributed to the co-occurrence of Sb^{5+} and Sb^{3+} states at higher Sb content [26,33,39]. The experimental conditions were reported to affect the Sb^{5+}/Sb^{3+} ratio and contribute to the formation of the Sb^{5+} and Sb^{3+} mixed valences [40,41]. The evolution of the oxidation state was well documented by XPS studies [35,40,41]. Fan et al. [35] determined the Sb^{5+}/Sb^{3+} ratio by calculating the area ratio of the 3d$_{5/2}$ and 3d$_{3/2}$ peaks on XPS spectra in Sb-doped SnO_2 ceramics obtained by hydrothermal method followed by sintering. The content of Sb^{5+} was higher than that of Sb^{3+} and the content of Sb^{5+} and the electrical conductivity in sintered ceramics increases almost linearly in a certain range. At higher doping content, the Sb^{5+} ratio is lower as well as the electrical conductivity. This is important for the transport properties, as Sb^{5+} ions act as electron donors and are responsible for higher conductivity. On the other hand, Sb^{3+} ions decrease the carrier concentration.

As shown in Fig. 4, the Seebeck coefficient in all the samples is negative over the entire measurement temperature range, confirming that the conduction mechanism is n-type and the electrons are the conductive carriers.

The absolute values of the Seebeck coefficient decreased with increasing Sb content as a consequence of the increased carrier concentration, as the Seebeck coefficient is inversely proportional to the charge carrier concentration of the samples. A slight increase in the Seebeck coefficient in samples with a higher amount of Sb was observed, due to the (experimentally observed) reduced mobility of charge carriers. The maximum values of -67 μV K^{-1} at 373 K and -114 μV K^{-1} at 1073 K of the $Sn_{0.995}Sb_{0.005}O_2$ sample are relatively low Seebeck coefficient values, for example in comparison to other Sb-doped SnO_2 as $Sn_{0.99}Sb_{0.01}O_2$ (~-155 μV K^{-1} at 1073 K) [26] and $Sn_{0.99}Sb_{0.01}O_2$ (-86 μV K^{-1} at room temperature) [25],and in comparison to other oxides as post-annealing Zn_2AlO_4 (-120 μV K^{-1} at room temperature), Zn_2SnO_4

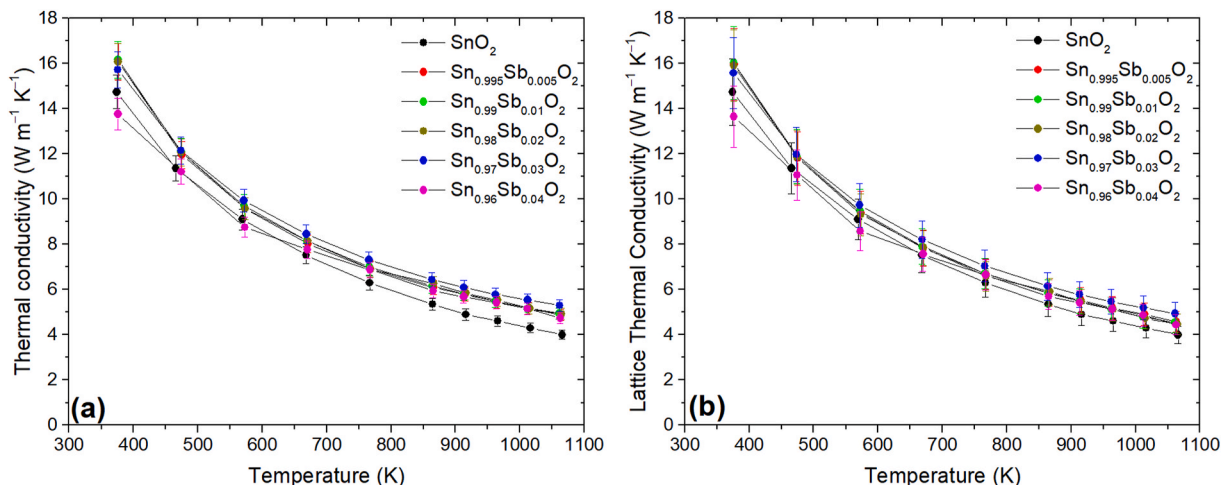**Fig. 5.** (a) Total thermal conductivity and (b) lattice thermal conductivity of $Sn_{1-x}Sb_xO_2$ (x = 0, 0.005, 0.01, 0.02, 0.03, 0.04).

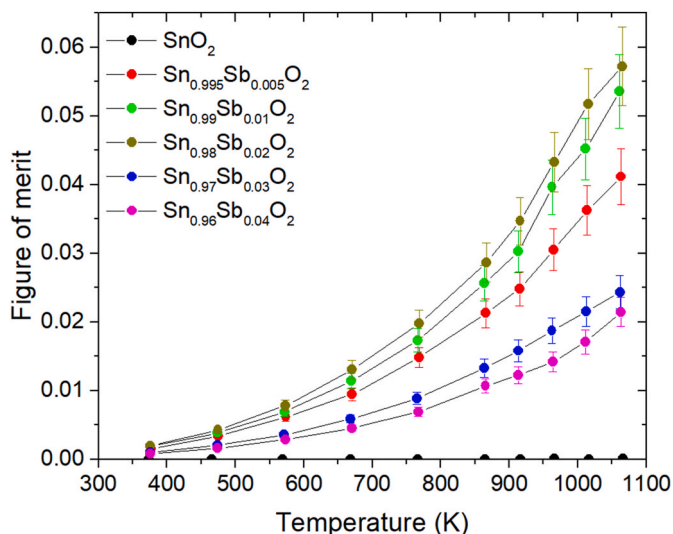**Fig. 6.** Figure of merit of $Sn_{1-x}Sb_xO_2$ (x = 0, 0.005, 0.01, 0.02, 0.03, 0.04).

(-148 µV K^{-1} at room temperature) [36], $In_{1.9}Mo_{0.1}O_3$ (~-375 µV K^{-1} at 1073 K) [37], $Ca_{0.96}Gd_{0.04}Mn_{0.96}Nb_{0.04}O_3$ (-150 µV K^{-1} at 800 K) and reasonably competitive in comparison to $Ca_{0.94}Gd_{0.06}Mn_{0.94}Nb_{0.06}O_3$ (-110 µV K^{-1} at 800 K) [42].

The power factor was calculated using the electrical conductivity and Seebeck coefficient values via $PF = S^2\sigma$ (Fig. S1). The maximum value of 0.8 µW cm^{-1}K^{-2} at 373 K and 2.7 µW cm^{-1}K^{-2} at 1073 K found for the $Sn_{0.98}Sb_{0.02}O_2$ sample is higher than the 1.20 µW cm^{-1}K^{-2} found for $Sn_{0.9}Sb_{0.05}Zn_{0.05}O_2$ at 1073 K [15], and <1 µW cm^{-1}K^{-2} at 1073 K for $Sn_{0.99}Sb_{0.01}O_2$ [27], and $\sim$1.6 µW cm^{-1}K^{-2} at 773 K for $Sn_{0.99}Sb_{0.01}O_2$ as recently reported by Zhao et al. [25] However, Rubenis et al. reported that the $Sn_{0.99}Sb_{0.01}O_2$ sample has a power factor value of 4.5 µW cm^{-1}K^{-2} at 1073 K [26]. Other n-type oxides with a wide bandgap, such as ZnO and In_2O_3 also showed relatively high power factors. Ohtaki et al. [43] obtained bulk $Zn_{0.96}Al_{0.02}Ga_{0.02}O$ via the solid-state method showing a large power factor value of 23.9 µW cm^{-1}K^{-2} at 1147 K. Liu et al. [44] prepared $In_{1.90}Ga_{0.10}O_3$ via spark plasma sintering, which achieved the highest power factor value of 9.6 µW cm^{-1}K^{-2} at 973 K. However, some other n-type oxides showed competitive or lower power factors like post-annealing Zn_2AlO_4 (0.8 µW cm^{-1}K^{-2} at room temperature), Zn_2SnO_4 (1.2 µW cm^{-1}K^{-2} at room temperature) [36], and $Ca_{0.94}Gd_{0.06}Mn_{0.94}Nb_{0.06}O_3$ ($\sim$1.4 µW cm^{-1}K^{-2} at 800 K) and $Ca_{0.96}Gd_{0.04}Mn_{0.96}Nb_{0.04}O_3$ (2.25 µW cm^{-1}K^{-2} at 800 K) [42].

The electronic contribution to the thermal conductivity can be determined using the Wiedemann Franz law $\kappa_e = LT\sigma$, where σ is the electrical conductivity, T the temperature and L the Lorenz number [45]. The single parabolic band model for the Seebeck coefficient was used to calculate the Lorenz number (Fig. S2) [46]. According to the formula $\kappa = \kappa_e + \kappa_L$, where κ_e is the electronic thermal conductivity, κ_L can be derived. κ_e has a small influence on the total thermal conductivity because of the relatively low electrical conductivity in the measured temperature range (Fig. S3) and accordingly κ_L is the predominant component in κ and the variation mainly arises from the alteration in κ_L

for SnO_2 materials, as depicted in Fig. 5.

As the measurement temperature increases from 373 K to 1073 K, the total thermal conductivities of all the samples show a constant decreasing trend. As the temperature increases, the scattering of phonons increases and thereby causes a reduction in heat transfer. The scattering mechanism arises due to the presence of impurities, grain boundaries or phonons in the lattice site [47]. All Sb-doped SnO_2 samples have lower or competitive thermal conductivity values ($\sim$4.7–5.3 W m^{-1}K^{-1} at 1073 K) in comparison to $Sn_{0.99}Sb_{0.01}O_2$ (6.6 W m^{-1}K^{-1} at 1073 K) [26], $Sn_{0.99}Sb_{0.01}O_2$ (4.2 W m^{-1}K^{-1} at 773 K) [25], $Zn_{0.96}Al_{0.02}Ga_{0.02}O$ ($\sim$5 W m^{-1}K^{-1} at 1073 K) [43], and $CaMnO_3$ (4 W m^{-1}K^{-1} at 873 K) [38]. The thermal conductivity values obtained for $In_{1.90}Ga_{0.10}O_3$ by Liu et al. [44] were slightly lower ($\sim$2.5 W m^{-1}K^{-1} at 973 K), and the ones for $Ca_{0.94}Gd_{0.06}Mn_{0.94}Nb_{0.06}O_3$ and $Ca_{0.96}Gd_{0.04}Mn_{0.96}Nb_{0.04}O_3$ by Nag et al. [42] (1.5 W m^{-1}K^{-1} at 800 K and 1.2 W m^{-1}K^{-1} at 800 K, respectively) were even lower. At low temperatures, the main scattering mechanism occurs due to the presence of impurity ions and grain boundaries, whereas at higher temperatures, the thermal conductivity of Sb-doped samples did not show any significant differences in dependence of the Sb content. The lower values of thermal conductivity of the pristine sample can be attributed to its slightly lower density.

Fig. 6 shows the dimensionless figure of merit zT calculated from the above-discussed properties. For all samples zT increases as temperature rises. The figure of merit is strongly enhanced by Sb addition, peaking for x = 0.02, the sample with the highest electrical conductivity.

The maximum value of the figure of merit for the $Sn_{0.98}Sb_{0.02}O_2$ sample is $\sim$0.06 at 1073 K. In comparison to leading n-type oxides with a wide bandgap, zT $\sim$0.06 at 1073 K is still a relatively low value of figure of merit. Ohtaki et al. [43] obtained zT values of 0.47 at 1000 K and 0.65 at 1247 K for $Zn_{0.96}Al_{0.02}Ga_{0.02}O$, and Liu et al. [44] achieved a maximum zT value of 0.37 at 973 K for $In_{1.90}Ga_{0.10}O_3$. Nag et al. [42] obtained a comparable value of 0.07 to $Ca_{0.94}Gd_{0.06}Mn_{0.94}Nb_{0.06}O_3$ and 0.15 to $Ca_{0.96}Gd_{0.04}Mn_{0.96}Nb_{0.04}O_3$. However, the equivalent value of zT $\sim$0.06 at 1073 K was found by Rubenis et al. [26] for the $Sn_{0.99}Sb_{0.01}O_2$ sample synthesized via spark plasma sintering and subsequent air annealing. In addition, Zhao et al. [25] obtained zT $\sim$ 0.05 at 773 K for $Sn_{0.99}Sb_{0.01}O_2$ synthesized via the hydrothermal method followed by spark plasma sintering, and Torres et al. [38] presented a maximum zT value of 0.03 at 873 K for $CaMnO_3$. Table 2 summarizes the thermoelectric properties at 1073 K of $Sn_{1-x}Sb_xO_2$ (x = 0, 0.005, 0.01, 0.02, 0.03, 0.04) samples obtained by one-step solid-state method. In summary, the one-step solid-state method proved to be a reliable and cheap method to synthesize Sb-doped tin oxide thermoelectric materials with a comparable figure of merit value.

5. Conclusion

SnO_2 and Sb-doped SnO_2 compounds were synthesized via a one-step solid-state reaction by changing the concentration of the dopants from 0 to 4 mol %. XRD analysis showed the phase purity of the synthesized material; the particle size was found to moderately decrease with an increase in doping concentration. Surface morphology examination with SEM scanning showed that the grains are closely packed and faceted particles were found in the antimony doped solid solution. The

Table 2
Thermoelectric properties of $Sn_{1-x}Sb_xO_2$ (x = 0, 0.005, 0.01, 0.02, 0.03, 0.04) solid solutions at 1073 K.

Nominal composition	σ (Ω^{-1}cm^{-1})	S (µVK^{-1})	PF (µWcm^{-1}K^{-2})	K_{total} (Wm^{-1}K^{-1})	$K_{electronic}$ (Wm^{-1}K^{-1})	$K_{lattice}$ (Wm^{-1}K^{-1})	zT
SnO_2	2E-3	-509	5E-4	4.0	0	4.0	1E-5
$Sn_{0.995}Sb_{0.005}O_2$	145	-114	1.9	4.9	0.3	4.6	0.04
$Sn_{0.99}Sb_{0.01}O_2$	194	-113	2.5	4.9	0.4	4.5	0.05
$Sn_{0.98}Sb_{0.02}O_2$	231	-108	2.7	4.9	0.5	4.4	0.06
$Sn_{0.97}Sb_{0.03}O_2$	169	-85	1.2	5.3	0.4	4.9	0.02
$Sn_{0.96}Sb_{0.04}O_2$	142	-82	1.0	4.7	0.3	4.4	0.02

thermoelectric properties measurements revealed that Sb-doped SnO_2 can be considered an acceptable candidate for thermoelectric application due to its increase in electrical conductivity. However, excessive addition of antimony is ineffective for the enhancement of the σ value due to the presence of Sb^{3+}. The thermoelectric performance of the material was evaluated by determining the zT value and the best composition was $Sn_{0.98}Sb_{0.02}O_2$.

Declaration of competing interest

The authors declare that they have no known competing financial interests or personal relationships that could have appeared to influence the work reported in this paper.

Acknowledgements

Appendix A. Supplementary data

Supplementary data to this article can be found online at https://doi.org/10.1016/j.ceramint.2021.10.137.

References

[1] H. Jouhara, N. Khordehgah, S. Almahmoud, B. Delpech, A. Chauhan, S.A. Tassou, Waste heat recovery technologies and applications, Therm. Sci. Eng. Prog. 6 (2018) 268–289, https://doi.org/10.1016/j.tsep.2018.04.017.

[2] J. He, T.M. Tritt, Advances in thermoelectric materials research: looking back and moving forward, Science 357 (2017) 1369–1378, https://doi.org/10.1126/science.aak9997.

[3] P. Ying, R. He, J. Mao, Q. Zhang, H. Reith, J. Sui, Z. Ren, K. Nielsch, G. Schierning, Towards tellurium-free thermoelectric modules for power generation from low-grade heat, Nat. Commun. 12 (2021), https://doi.org/10.1038/s41467-021-21391-1.

[4] G.J. Snyder, A.H. Snyder, Figure of merit ZT of a thermoelectric device defined from materials properties, Energy Environ. Sci. 10 (2017) 2280–2283, https://doi.org/10.1039/c7ee02007d.

[5] A. Assoud, H. Kleinke, Metal pnictides: structures and thermoelectric properties, in: R. Dronskowski, S. Kikkawa, Andreas Stein (Eds.), Handb. Solid State Chem., Wiley-VCH, Weinheim, Germany, 2017, pp. 455–476, https://doi.org/10.1002/9783527691036.hsscvol1012.

[6] X. Shen, Y. Xia, C.C. Yang, Z. Zhang, S. Li, Y.H. Tung, A. Benton, X. Zhang, X. Lu, G. Wang, J. He, X. Zhou, High thermoelectric performance in sulfide-type Argyrodites compound $Ag_8Sn(S_{1-x}Se_x)_6$ enabled by ultralow lattice thermal conductivity and extended cubic phase regime, Adv. Funct. Mater. 30 (2020) 1–10, https://doi.org/10.1002/adfm.202000526.

[7] P. Jafarzadeh, M.R. Rodrigues, Y. Shi, A. Assoud, T. Zou, J.B. Kycia, H. Kleinke, Effect of mixed occupancies on the thermoelectric properties of $BaCu_{6-x}Se_{1-y}Te_{6+y}$ polychalcogenides, Dalton Trans. 48 (2019) 9357–9364, https://doi.org/10.1039/c9dt01616c.

[8] G. Yang, L. Sang, M. Li, S.M. Kazi Nazrul Islam, Z. Yue, L. Liu, J. Li, D.R.G. Mitchell, N. Ye, X. Wang, Enhancing the thermoelectric performance of polycrystalline SnSe by decoupling electrical and thermal transport through carbon fiber incorporation, ACS Appl. Mater. Interfaces 12 (2020) 12910, https://doi.org/10.1021/acsami.0c00873, 12918.

[9] W. Lu, X. Lai, Q. Liu, Z. He, H. Zhao, J. Jian, Enhanced thermoelectric performance of BiSe by Sn doping and ball milling, Ceram. Int. 47 (2021) 26375–26382, https://doi.org/10.1016/j.ceramint.2021.06.048.

[10] M.N. Hasan, H. Wahid, N. Nayan, M.S. Mohamed Ali, Inorganic thermoelectric materials: a review, Int. J. Energy Res. 44 (2020) 6170–6222, https://doi.org/10.1002/er.5313.

[11] Y. Feng, X. Jiang, E. Ghafari, B. Kucukgok, C. Zhang, I. Ferguson, N. Lu, Metal oxides for thermoelectric power generation and beyond, Adv. Compos. Hybrid Mater. 1 (2018) 114–126, https://doi.org/10.1007/s42114-017-0011-4.

[12] J.A. Hernandez, J. Carpena-Nunez, L.F. Fonseca, M.T. Pettes, M.J. Yacaman, A. Benitez, Thermoelectric properties and thermal tolerance of indium tin oxide nanowires, Nanotechnology 29 (7pp) (2018) 364001, https://doi.org/10.1088/1361-6528/aaccd3.

[13] P. Zhu, T. Takeuchi, H. Ohta, W.S. Seo, K. Koumoto, Preparation and thermoelectric properties of Na_xCoO_2/Co_3O_4 layered nano-composite, Mater. Trans. 46 (2005) 1453–1455, https://doi.org/10.2320/matertrans.46.1453.

[14] J.H. Lin, C.S. Hwang, F.R. Sie, Preparation and thermoelectric properties of Nd and Dy co-doped $SrTiO_3$ bulk materials, Mater. Res. Bull. 122 (2020) 3–10, https://doi.org/10.1016/j.materresbull.2019.110650.

[15] S.I. Yanagiya, S. Furuyama, I. Uriya, M. Takeda, Thermoelectric properties of SnO_2 ceramics codoped with Sb and Zn prepared by reactive spark plasma synthesis followed by thermal treatment, Sensor. Mater. 27 (2015) 917–924, https://doi.org/10.18494/sam.2015.1155.

[16] S. Yanagiya, N.V. Nong, M. Sonne, N. Pryds, Thermoelectric properties of SnO_2-based ceramics doped with Nd, Hf or Bi, AIP Conf. Proc. 1449 (2012) 327–330, https://doi.org/10.1063/1.4731563.

[17] S. Das, V. Jayaraman, SnO, A comprehensive review on structures and gas sensors, Prog. Mater. Sci. 66 (2014) 112–255, https://doi.org/10.1016/j.pmatsci.2014.06.003.

[18] E.J.H. Lee, C. Ribeiro, T.R. Giraldi, E. Longo, E.R. Leite, J.A. Varela, Photoluminescence in quantum-confined SnO_2 nanocrystals: evidence of free exciton decay, Appl. Phys. Lett. 84 (2004) 1745–1747, https://doi.org/10.1063/1.1655693.

[19] J. Yan, Y. Chen, X. Wang, Y. Fu, J. Wang, J. Sun, G. Dai, S. Tao, Y. Gao, High-performance solar-blind SnO_2 nanowire photodetectors assembled using optical tweezers, Nanoscale 11 (2019) 2162–2169, https://doi.org/10.1039/c8nr07382a.

[20] J.A. Smith, O.S. Game, J.E. Bishop, E.L.K. Spooner, R.C. Kilbride, C. Greenland, R. Jayaprakash, T.I. Alanazi, T.I. Alanazi, E.J. Cassella, A. Tejada, A. Tejada, G. Chistiakova, M. Wong-Stringer, T.J. Routledge, A.J. Parnell, D.B. Hammond, D. G. Lidzey, Rapid scalable processing of tin oxide transport layers for perovskite solar cells, ACS Appl. Energy Mater. 3 (2020) 5552–5562, https://doi.org/10.1021/acsaem.0c00525.

[21] E.R. Leite, I.T. Weber, E. Longo, J.A. Varela, New method to control particle size and particle size distribution of SnO_2 nanoparticles for gas sensor applications, Adv. Mater. 12 (2000) 965–968, https://doi.org/10.1002/1521-4095(200006)12:13<965::AID-ADMA965>3.0.CO;2-7.

[22] G.H. Patel, S.H. Chaki, R.M. Kannaujiya, Z.R. Parekh, A.B. Hirpara, A.J. Khimani, M.P. Deshpande, Sol-gel synthesis and thermal characterization of SnO_2 nanoparticles, Phys. B Condens. Matter 613 (2021) 412987/9, https://doi.org/10.1016/j.physb.2021.412987.

[23] D.C. Onwudiwe, Nano-sized SnO_2 by a facile nanosecond laser irradiation in aqueous solution, Mater. Res. Express 6 (2019), 125004/6, https://doi.org/10.1088/2053-1591/ab52ba.

[24] B. Yu, Y. Li, Y. Wang, H. Li, R. Zhang, Facile hydrothermal synthesis of SnO_2 quantum dots with enhanced photocatalytic degradation activity: role of surface modification with chloroacetic acid, J. Environ. Chem. Eng. 9 (2021), 105618/13, https://doi.org/10.1016/j.jece.2021.105618.

[25] X.D. Zhao, S.P. Deng, W.F. Pan, N. Qi, Z.Q. Chen, X.L. Su, X.F. Tang, Enhanced thermoelectric performance of tin oxide through antimony doping and introducing pore structures, J. Mater. Sci. 56 (2021) 2360–2371, https://doi.org/10.1007/s10853-020-05291-1.

[26] K. Rubenis, S. Populoh, P. Thiel, S. Yoon, U. Müller, J. Locs, Thermoelectric properties of dense Sb-doped SnO_2 ceramics, J. Alloys Compd. 692 (2017) 515–521, https://doi.org/10.1016/j.jallcom.2016.09.062.

[27] T. Tsubota, S. Kobayashi, N. Murakami, T. Ohno, Improvement of thermoelectric performance for Sb-doped SnO_2 ceramics material by addition of Cu as sintering additive, J. Electron. Mater. 43 (2014) 3567–3573, https://doi.org/10.1007/s11664-014-3227-x.

[28] J.A. Varela, L.A. Perazolli, E. Longo, E.R. Leite, J.A. Cerri, Effect of atmosphere and dopants on sintering of SnO_2, Radiat. Eff. Defect Solid 146 (1998) 131–143, https://doi.org/10.1080/10420159808220286.

[29] B.H. Toby, H.S. R, A.F. H, B.I. D, R.H. M, U.L. M, U.A. G, U.L. M, U.A. G, U.L. M, U. A. G, *EXPGUI*, a graphical user interface for *GSAS*, J. Appl. Crystallogr. 34 (2001) 210–213, https://doi.org/10.1107/S0021889801002242.

[30] A.C. Larson, R.B. von Dreele, General Structure Analysis System (GSAS), Los Alamos National Laboratory, Los Alamos, 2000.

[31] D. Szczuko, J. Werner, S. Oswald, G. Behr, K. Wetzig, XPS investigations of surface segregation of doping elements in SnO_2, Appl. Surf. Sci. 179 (2001) 301–306, https://doi.org/10.1016/S0169-4332(01)00298-7.

[32] G.B. González, Investigating the defect structures in transparent conducting oxides using X-ray and neutron scattering techniques, Materials 5 (2012) 818–850, https://doi.org/10.3390/ma5050818.

[33] V. Müller, M. Rasp, G. Štefanić, J. Ba, S. Günther, J. Rathousky, M. Niederberger, D. Fattakhova-Rohlfing, Highly conducting nanosized monodispersed antimony-doped tin oxide particles synthesized via nonaqueous sol-gel procedure, Chem. Mater. 21 (2009) 5229–5236, https://doi.org/10.1021/cm902189r.

[34] M.R. Fadavieslam, Effect of Sb doping on the structural, electrical, and optical properties of SnO_2 thin films prepared through spray pyrolysis, J. Mater. Sci. Mater. Electron. 27 (2016) 4943–4950, https://doi.org/10.1007/s10854-016-4379-7.

[35] G. Fan, Z. Wang, K. Sun, Y. Liu, R. Fan, Doping-dependent negative dielectric permittivity realized in mono-phase antimony tin oxide ceramics, J. Mater. Chem. C. 8 (2020) 11610–11617, https://doi.org/10.1039/d0tc02266g.

[36] J. Jacob, U. Rehman, K. Mahmood, A. Ali, K. Mehboob, A. Ashfaq, S. Ikram, N. Amin, S. Hussain, F. Ashraf, Improved thermoelectric performance of Al and Sn doped ZnO nano particles by the engineering of secondary phases, Ceram. Int. 46 (2020) 15013–15017, https://doi.org/10.1016/j.ceramint.2020.03.031.

[37] W. Klich, M. Ohtaki, Thermoelectric properties of Mo-doped bulk In_2O_3 and prediction of its maximum ZT, Ceram. Int. 47 (2021) 18116–18121, https://doi.org/10.1016/j.ceramint.2021.03.129.

[38] S.O.A. De Torres, D. Thomazini, G.P. Balthazar, M.V. Gelfuso, Microstructural influence on thermoelectric properties of CaMnO$_3$ ceramics, Mater. Res. 23 (2021), https://doi.org/10.1590/1980-5373-MR-2020-0169.

[39] C. Terrier, J.P. Chatelon, R. Berjoan, J.A. Roger, Sb-doped SnO$_2$ transparent conducting oxide from the sol-gel dip-coating technique, Thin Solid Films 263 (1995) 37–41, https://doi.org/10.1016/0040-6090(95)06543-1.

[40] Y.M. Cross, D.R. Pyke, An X-ray photoelectron spectroscopy study of the surface composition of tin and antimony mixed metal oxide catalysts, J. Catal. 58 (1979) 61–67, https://doi.org/10.1016/0021-9517(79)90244-6.

[41] D. Dobler, S. Oswald, J. Werner, W. Arabczyk, G. Behr, K. Wetzig, X-ray photoelectron spectroscopy investigation of segregation processes at Sb and in doped SnO$_2$, Chem. Phys. 286 (2003) 375–383, https://doi.org/10.1016/S0301-0104(02)00970-9.

[42] A. Nag, F. D'Sa, V. Shubha, Doping induced high temperature transport properties of Ca$_{1-x}$Gd$_x$Mn$_{1-x}$Nb$_x$O$_3$ (0 $\leq$ x $\leq$ 0.1), Mater. Chem. Phys. 151 (2015) 119–125, https://doi.org/10.1016/j.matchemphys.2014.11.045.

[43] M. Ohtaki, K. Araki, K. Yamamoto, High thermoelectric performance of dually doped ZnO ceramics, J. Electron. Mater. 38 (2009) 1234–1238, https://doi.org/10.1007/s11664-009-0816-1.

[44] Y. Liu, W. Xu, D.B. Liu, M. Yu, Y.H. Lin, C.W. Nan, Enhanced thermoelectric properties of Ga-doped In$_2$O$_3$ ceramics via synergistic band gap engineering and phonon suppression, Phys. Chem. Chem. Phys. 17 (2015) 11229–11233, https://doi.org/10.1039/c5cp00739a.

[45] G.V. Chester, A. Thellung, The law of Wiedemann and Franz, Proc. Phys. Soc. 77 (1961) 1005–1013, https://doi.org/10.1088/0370-1328/77/5/309.

[46] X. Wang, V. Askarpour, J. Maassen, M. Lundstrom, On the calculation of Lorenz numbers for complex thermoelectric materials, J. Appl. Phys. 123 (2018), https://doi.org/10.1063/1.5009939, 055104/9.

[47] E.R. Leite, J.A. Cerri, E. Longo, J.A. Varela, Sintering of undoped SnO$_2$, Cerâmica 49 (2003) 87–91, https://doi.org/10.1590/s0366-69132003000200005.